Bioactive Materials 41 (2024) 427–439

Contents lists available at ScienceDirect

Bioactive Materials

journal homepage: www.keaipublishing.com/en/journals/bioactive-materials

Personalized composite scaffolds for accelerated cell- and growth factor-free craniofacial bone regeneration

Mirae Kim [a,b], Xinlong Wang [a,b], Yiming Li [c], Zitong Lin [c], Caralyn P. Collins [b,d], Yugang Liu [a,b], Yujin Ahn [e], Hsiu-Ming Tsal [f], Joseph W. Song [a,b], Chongwen Duan [a,b], Yi Zhu [g], Cheng Sun [b,d], Tong-Chuan He [b,g], Yuan Luo [c,h,i], Russell R. Reid [b,j,**], Guillermo A. Ameer [a,b,k,l,m,*]

[a] Department of Biomedical Engineering, Northwestern University, Evanston, IL, 60208, USA
[b] Center for Advanced Regenerative Engineering, Northwestern University, Evanston, IL, 60208, USA
[c] Department of Preventive Medicine, Feinberg School of Medicine, Northwestern University, Chicago, IL, 60611, USA
[d] Department of Mechanical Engineering, Northwestern University, Evanston, IL, 60208 USA
[e] Department of Chemical and Biomolecular Engineering, University of Illinois at Urbana-Champaign, Urbana, IL, 61820, USA
[f] Department of Radiology, The University of Chicago, Chicago, IL, 60637, USA
[g] Molecular Oncology Laboratory, Department of Orthopedic Surgery and Rehabilitation Medicine, The University of Chicago Medical Center, Chicago, IL, 60637, USA
[h] Clinical and Translational Sciences Institute, Northwestern University, Chicago, IL, 60611, USA
[i] Center for Collaborative AI in Healthcare, Institute for AI in Medicine, Northwestern University, Chicago, IL, 60611, USA
[j] Laboratory of Craniofacial Biology and Development, Section of Plastic and Reconstructive Surgery, Department of Surgery, The University of Chicago Medical Center, Chicago, IL, 60637, USA
[k] Department of Surgery, Feinberg School of Medicine, Northwestern University, Chicago, IL, 60611, USA
[l] Chemistry of Life Process Institute, Northwestern University, Chicago, IL, 60208, USA
[m] International Institute for Nanotechnology, Northwestern University, Evanston, IL, 60208, USA

ARTICLE INFO

Keywords:
Craniofacial bone regeneration
Composite scaffold
Material-centric approach
3D printing
Citrate biomaterial

ABSTRACT

Approaches to regenerating bone often rely on integrating biomaterials and biological signals in the form of cells or cytokines. However, from a translational point of view, these approaches are challenging due to the sourcing and quality of the biologic, unpredictable immune responses, complex regulatory paths, and high costs. We describe a simple manufacturing process and a material-centric 3D-printed composite scaffold system (CSS) that offers distinct advantages for clinical translation. The CSS comprises a 3D-printed porous polydiolcitrate-hydroxyapatite composite elastomer infused with a polydiolcitrate-graphene oxide hydrogel composite. Using a micro-continuous liquid interface production 3D printer, we fabricate a precise porous ceramic scaffold with 60 wt% hydroxyapatite resembling natural bone. The resulting scaffold integrates with a thermoresponsive hydrogel composite *in situ* to fit the defect, which is expected to enhance surface contact with surrounding tissue and facilitate biointegration. The antioxidative properties of citrate polymers prevent long-term inflammatory responses. The CSS stimulates osteogenesis *in vitro* and *in vivo*. Within 4 weeks in a calvarial critical-sized bone defect model, the CSS accelerated ECM deposition (8-fold) and mineralized osteoid (69-fold) compared to the untreated. Through spatial transcriptomics, we demonstrated the comprehensive biological processes of CSS for prompt osseointegration. Our material-centric approach delivers impressive osteogenic properties and streamlined manufacturing advantages, potentially expediting clinical application for bone reconstruction surgeries.

1. Introduction

There are approximately 3 million cases of craniofacial trauma reported each year in the United States, constituting all 21 % of significant traumatic injuries [1]. Craniofacial bone defects resulting from traumatic injuries present with unique challenges for patients and

Peer review under responsibility of KeAi Communications Co., Ltd.
* Corresponding author. Department of Biomedical Engineering, Northwestern University, Evanston, IL, 60208, USA.
** Corresponding author. Laboratory for Craniofacial Biology and Development, Section of Plastic and Reconstructive Surgery, Department of Surgery, The University of Chicago Medical Center, Chicago, IL, 60637, USA.
E-mail addresses: rreid@bsd.uchicago.edu (R.R. Reid), g-ameer@northwestern.edu (G.A. Ameer).

https://doi.org/10.1016/j.bioactmat.2024.07.029
Received 29 January 2024; Received in revised form 16 July 2024; Accepted 21 July 2024
2452-199X/© 2024 The Authors. Publishing services by Elsevier B.V. on behalf of KeAi Communications Co. Ltd. This is an open access article under the CC BY-NC-ND license (http://creativecommons.org/licenses/by-nc-nd/4.0/).

surgeons, necessitating complex surgeries and substantial surgical costs [2]. Autografts, while considered the gold standard for craniofacial reconstruction surgery [3,4], bring challenges such as the need for a second/donor surgical site, prolonged operative time, and increased patient discomfort and recovery. Bone tissue engineering has been considered a promising alternative, aiming to replicate the native craniofacial environment without complex technical demands [5]. However, integrating biological components such as stem cells and growth factors increases regulatory complexity [6], raises product development costs, and can elicit unwanted immune and inflammatory responses [7,8]. In this regard, material-centric approaches offer significant potential for accelerating commercialization strategies and improving patient outcomes [5,9].

Additive manufacturing using continuous liquid interface production (CLIP) offers advantages in printing speed and complex architecture fabrication at high resolutions [10,11]. Therefore, a 3D-printed scaffold system developed using CLIP technology has significant potential advantages in complex cranial bone reconstruction [12]. Nevertheless, for defects larger than a critical size, inadequate blood supply and slow tissue integration can lead to fibrous tissue formation at the center of the defect instead of regenerated bone [13,14]. This problem significantly reduces the likelihood of complete osseointegration and successful bone healing, presenting an unmet clinical need [13]. Therefore, the scaffold system should not only conform to the defect geometry in 3D but also provide a microenvironment conducive to osteogenesis and angiogenesis to achieve successful regeneration in critical-sized bone defects [15].

Several material-centric strategies have proposed composite scaffold systems (**CSS**) to accelerate osteogenesis and angiogenesis, either by integrating ceramics with hydrogels [16] or by combining them with polymers and additives (e.g., bioactive particles or graphene derivatives) [17,18]. However, the low solubility of ceramics under physiological conditions leads to poor interface interaction with hydrogels, causing structural instability; and employing particles for enhancing miscibility [19,20] might compromise biocompatibility. Moreover, the mechanical properties of porous ceramic scaffolds can be influenced by the quantity of additives [17,21], complicating the independent manipulation of structural and functional properties.

Herein, we present a customizable CSS comprised of biphasic citrate-based polymers, incorporating two microparticles, hydroxyapatite (**HA**) and graphene oxide (**GO**). This CSS is developed by integrating a polydiolcitrate-GO hydrogel composite (**GP hydrogel**) into a 3D-printed porous polydiolcitrate-HA (P-HA) scaffold. The 3D-printed P-HA scaffold utilizes a poly(1,8-octanediol citrate) (POC) citrate elastomer used in an FDA-cleared implantable medical device used for soft tissue fixation to bone [22]. The GP hydrogel enables *in situ* fabrication to precisely match the defect site [23] and enhances surface contact with the surrounding bone defect [24,25]. Furthermore, GO facilitates cell adhesion [26,27] and synergizes with HA to promote the absorption of Ca^{2+} and mineralization [28,29]. Consequently, the integrated GP hydrogel is expected to accelerate early tissue integration and osteogenesis. Additionally, the unique antioxidative properties of citrate-based polymers [30,31] are anticipated to prevent chronic inflammation.

We show that our CSS stimulates osseointegration with angiogenesis and osteogenesis of endogenous progenitors in a critical-sized defect model in rodents. Using spatial transcriptomics, we unveil potential mechanisms of action for CSS, including immune processes involved in early bone regeneration. From a clinical application perspective, our material design and strategy simplify complex considerations and facilitate patient translation and scalable manufacturing, indicating a promising advanced CSS for addressing cranial defects.

2. Results

2.1. GP hydrogel integrates into P-HA enabling CSS fabrication

The 3D-printed porous ceramic scaffolds are customized to fit a mouse skull defect model via a micro-continuous liquid interface production (μCLIP) 3D printer (Fig. 1A). Within this system, the composite mixture is placed in a resin bath, allowing photopolymerization by UV light penetration through an O_2-permeable window. Subsequently, the composite is additively manufactured by patterning UV light into cross-sectional images of the 3D-designed scaffold via a digital micromirror device (DMD). Following the printing, the hybrid CSS is fabricated by injecting the hydrogel-GO precursor solution into the structure and gelling it at 37 °C. The combination of 3D printing technology [10,11] and the injectable thermoresponsive hydrogel [32,33] allows for the convenient and swift fabrication of a customizable soft-rigid hybrid system.

The methacrylated poly(1,8-octanediol-citrate) (**mPOC**) was used as a 3D printable polymer and developed from POC via two steps (Fig. 1B). Initially, the POC was obtained through an esterification reaction between 1,8-octanediol and citric acid [34]. Subsequently, it was developed into mPOC by introducing methacrylate functional groups through a ring-opening reaction of glycidyl methacrylate. The chemical composition of mPOC was confirmed through ^{1}H-NMR and FT-IR spectroscopy analysis (Fig. S1). The ^{1}H-NMR analysis identified peaks at 1.9, 5.7, and 6 ppm, indicating the presence of methacrylate groups within the mPOC structure. The estimated molar ratio of citric acid to methacrylate was approximately 1:0.9, as inferred from the spectrum. In addition, the FT-IR spectrum exhibited a C=C stretching vibration peak at 1636 cm^{-1}. These results collectively demonstrate the effective modification of POC through methacrylation, allowing for radical polymerization under UV light throughout the 3D printing process.

The formulation of the composite involved a mixture of mPOC with HA microparticles (**P-HA**) (Fig. 1C). In order to achieve a wide range of 3D printable composite, we incorporated 2.5 μm HA (specific surface area, ≥80 m^2/g). A previous study has demonstrated that materials derived from HA exhibit cytocompatibility with stem cells and promote the osteogenic differentiation of such cells [35]. The incorporation of HA microparticles improved the viscosity of the composite, thereby enhancing its printability and allowing for HA contents of up to 60 %.

Poly (polyethylene glycol citrate-co-N-isopropylacrylamide) (**PPCN**) was used as the thermoseponsive hydrogel component (Fig. 1D). It was obtained with citric acid, PEG and N-isopropylacrylamide (**NIPAAm**) components [33], and due to the unique properties of the NIPAAm, it exhibits a lower critical solution temperature (LCST) that enables phase change from liquid to gel at physiological body temperature (37 °C) [36]. The ^{1}H-NMR spectrum of PPCN exhibited multiple peaks associated with citric acid, PEG, and NIPAAm units (Fig. S2). As a result of analyzing the signal intensity, the molar ratio between citric acid and poly (NIPAAm) was determined to be approximately 1:12, reflecting the molar feed ratio during synthesis. The FT-IR spectrum revealed that PPCN had characteristic amide peaks present in the NIPAAm structure, along with additional peaks indicating C=O, C-O, and -OH functional groups, attributed to citric acid, ester bonds and PEG (Fig. S2).

The PPCN was combined with gelatin (PPCNg) and then developed into GO-PPCNg (**GP**) hydrogel composite using the following method [37]. In brief, the PPCN was dissolved in PBS and blended with gelatin in a 1:1 ratio. Afterward, this mixture was combined with GO solution at a volume ratio of 5:1 (Fig. 1E). The physical appearance of GP hydrogel demonstrated favorable mixing of GO with PPCNg (Fig. 1F). It exhibited the LCST behavior typical of PPCN, remaining in a liquid state at 4 °C but undergoing a rapid gelation process at 37 °C, while GO solution consistently remained in a liquid form.

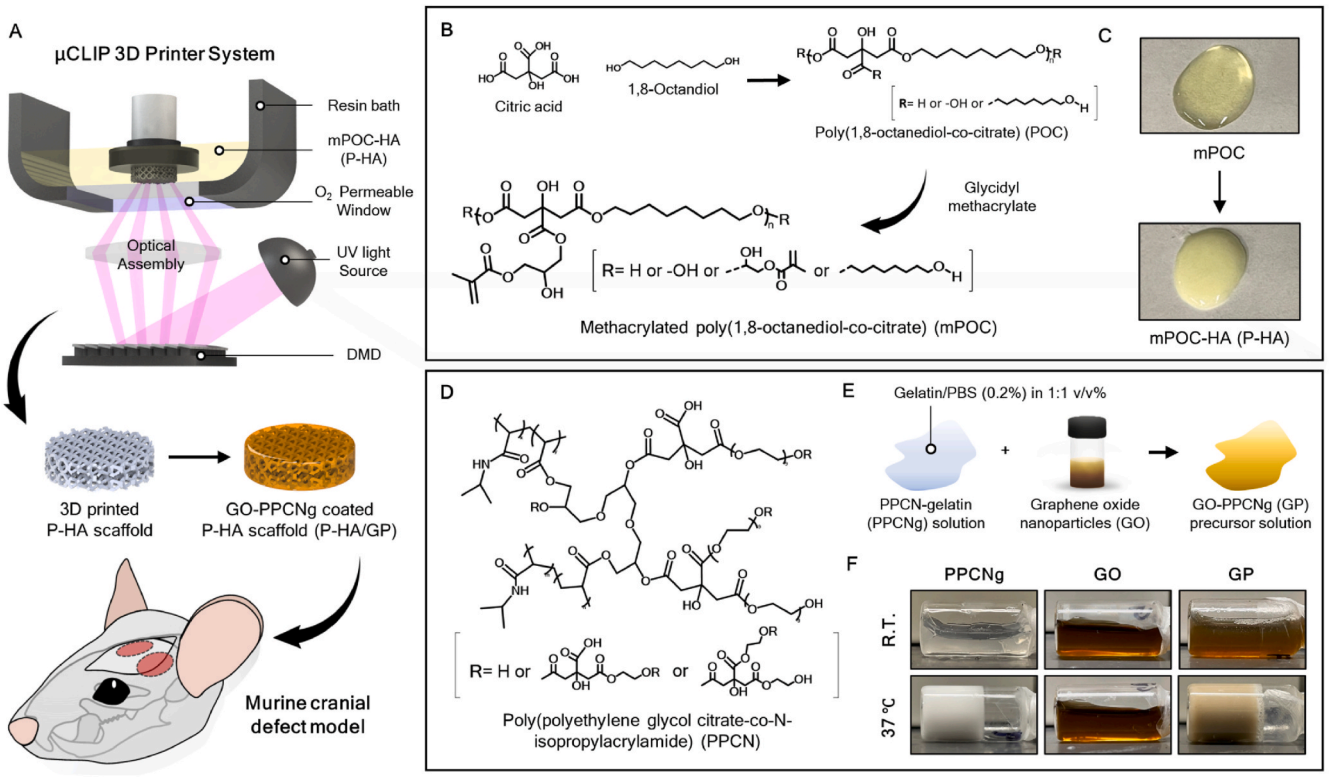

Fig. 1. Representative images of the 3D-printed CSS fabrication and preparation of P-HA and GP hydrogel. (**A**) μCLIP 3D printer system and schematic depiction of 3D-printed CSS implantation in cranial defect model. (**B**) Synthesis schematic of mPOC and its structure. (**C**) Preparation of P-HA composite consisting of mPOC polymer and HA. (**D**) Structure of PPCN and (**E**) schematic illustration of GP precursor solution preparation. (**F**) Different physiological properties of GO (0.4 mg/mL), PPCNg (50 mg/mL), and GP hybrid hydrogel at room temperature and 37 °C.

2.2. HA and GO improve mechanical and rheological properties of the scaffold

The combination of mPOC and HA provides processing flexibility, rendering it an ideal composite for fabricating 3D-printed porous structures of various dimensions and pore unit cell configurations using the μCLIP 3D printer (Fig. S3). For the subsequent experiments, the P-HA was engineered with a porous architecture featuring hexagonal unit cells

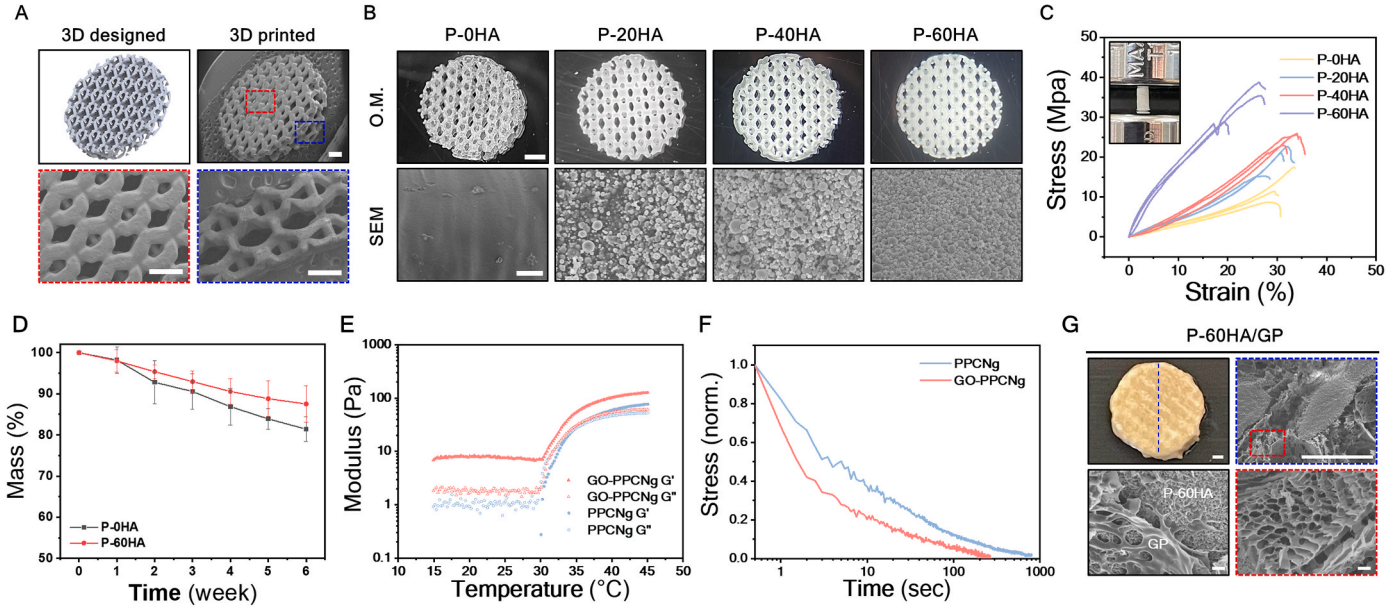

Fig. 2. Fabrication of 3D-printed porous P-HA scaffolds and characterization of P-HA scaffolds and GP hydrogel. (**A**) Comparison images between 3D design and 3D-printed P-HA scaffold. Scale bars, 500 μm. (**B**) 3D-printed P-HA scaffolds with various HA concentrations and morphological surface appearance of each scaffold in SEM. Scale bar, 1 mm (top) and 10 μm (bottom). (**C**) Representative stress-strain curves of each P-HA scaffold. n = 3 (**D**) Degradation behavior of each P-HA scaffold at 37 °C. Error bars, ±SD; n = 3. (**E**) Gelation kinetics of PPCNg and GP hydrogel, and (**F**) their stress-relaxation profiles at 37 °C. (**G**) Morphological structure of P-60HA/GP composite scaffold and GP hydrogel in SEM images. Scale bars, 500 μm (top) and 10 μm (bottom).

(Fig. 2A and Fig. S4).

The hexagonal structural element efficiently disperses external forces, enhancing the stability of the scaffolds [38,39]. Additionally, smaller internal pore units (<450 μm) (Fig. S4) aimed to promote osteogenesis and vascularization [40,41] while enabling the advantageous integration of the GP hydrogel throughout the scaffold. The μCLIP printer enabled precise customization by replicating the scaffold at a high resolution according to the designed structure without any pore blockages (Fig. 2A). The P-HA composite material was prepared at various HA concentrations ranging from 0 % to 60 % to evaluate mechanical properties according to HA content, which were labeled as P-0HA, P-20H, P-40H, and P-60HA depending on the content. Even with high HA content (60 wt%), the P-HA exhibited favorable printability characteristics (Fig. S3), and HA particles were distributed throughout the structure, as depicted in SEM (Fig. 2B). The surface roughness resulting from the addition of HA can promote cell adhesion [42] and differentiation [43,44]. Therefore, we expected that the surface properties of the P-HA scaffold would provide an advantage in osteogenesis.

In order to assess mechanical properties, the P-HA material was made into plug-shaped samples (3mm × 6 mm), which is a standard structure (ASTM D695) for measuring the compressive modulus of materials (Fig. 2C). The samples were measured using a universal testing machine until they fractured under a compressive load. Despite the potential impact of higher HA content on sample brittleness, the P-60HA exhibited enhancement in compressive strength (23.7 ± 1.6 MPa) (Fig. S5). This enhancement confirms the structural stability of the P-HA composite material, signifying compatibility between mPOC and HA (Fig. 2B). The P-HA scaffolds containing mPOC, comprised of biodegradable polyester chains, undergo hydrolysis *in vivo* leading to degradation [45]. The degradation behavior of 3D-printed porous P-HA scaffolds was investigated in PBS for 6 weeks at 37 °C (Fig. 2D and Fig. S6A). At 6 weeks, the P-0HA exhibited a mass loss of approximately 18.6 %, while that of P-60HA was 12.5 % (Fig. 2D).

We examined the impact of GO on the rheological and viscoelastic properties of the PPCNg hydrogel (Fig. 2E and F). The PPCNg hydrogels showed a phase transition from liquid to gel at 35 °C, where G″ and G′ intersected (Fig. 2E). While the GP hydrogel did not show a distinct intersection point, it exhibited a transition from liquid to gel above 35 °C (Fig. 1E). Furthermore, the GP hydrogel displayed gel-like characteristics with higher G′ values even in the liquid phase (below 35 °C) and improved the G′ of the PPCNg hydrogel from 77 to 126 Pa following the phase transition. This behavior is attributed to the interactions between GO and PPCNg chains within the GP mixture [37]. The stress relaxation of the hydrogels was investigated at 37 °C, maintaining a constant shear strain of 15 %, comparable to the strain applied by cells within a 3D matrix [46,47] (Fig. 2F). The GP hydrogel showed a faster half-stress relaxation time ($t_{1/2}$ ≈1.5 s) compared to PPCNg hydrogel ($t_{1/2}$ ≈3 s), which is likely due to GO particles interfering with the crosslinking of PPCN chains, leading to faster chain relaxation.

The P-60HA scaffold was combined with GP hydrogel, and the resulting hybrid CSS (**P-60HA/GP**) maintained a stable composite structure at 37 °C (Fig. 2G) without compromising mechanical strength (Fig. S7). The morphological structure and the distribution of GP hydrogel within the CSS were evaluated via SEM analysis (Fig. 2G). The GP hydrogel formed an extensive network by physically interacting with the P-60HA scaffold and uniformly covered the entire structure. Additionally, the GP hydrogel exhibited permeable porous channels supporting blood vessel formation and tissue ingrowth.

We confirmed that both the P-60HA scaffold and GP hydrogel collectively enhance physical properties, and the hybrid CSS demonstrated a consistent and durable structure. In subsequent experiments, the P-60HA scaffold was chosen as the primary structural framework of the CSS based on results, demonstrating improved mechanical properties with comparable mineral concentration to native bone (65-70 wt%).

2.3. P-60HA/GP is cytocompatible and promotes osteogenesis in vitro

We investigated the cytotoxicity and the *in vitro* osteogenic potential of the scaffolds using human mesenchymal stromal cells (hMSCs) (Fig. 3). To evaluate the influence of HA and GP hydrogel on cellular activity, the P-0HA, P-60HA, and P-60HA/GP scaffolds were examined, and each value was normalized to a TCP control group (Fig. 3A and B). The scaffolds were immersed in the TCP cultured with hMSCs for 7 days and subjected to live/dead staining (Fig. 3A) and alamarBlue assay (Fig. 3B). There were no observable dead cells, with sustained live cell proliferation, and cell viability was recorded at ≈90 % for 7 days, suggesting that both P-HA scaffolds and GP hydrogel are biocompatible.

The interaction between scaffolds and cells plays a crucial role as it enhances tissue reconstruction by enabling effective interaction with surrounding tissues post-implantation [48,49]. We assessed cell adhesion and retention on the scaffolds using cytoskeleton staining (Fig. 3C). hMSCs were cultured on P-60HA and P-60HA/GP for 4 days without cell adhesion treatment. In the staining results, P-60HA exhibited cell attachment, but cells had limited proliferation on the scaffold surface. In contrast, cells showed widespread distribution within the GP hydrogel of P-60HA/GP. This indicates that GP hydrogel provides a conducive microenvironment to cell growth, allowing cells to proliferate throughout the GP hydrogel-conjugated scaffold.

To demonstrate the effects of HA and GP hydrogel on the osteogenic differentiation of hMSCs, we analyzed osteogenesis markers at 7, 14, and 21 days after cell culturing on the scaffolds. First, the early osteogenic marker alkaline phosphatase (ALP) was assessed using the absorbance method and normalized to the DNA concentration of each group at the indicated time points (Fig. 3D). At day 7, ALP activity was significantly upregulated in P-60HA and P-60HA/GP compared to P-0HA. Moreover, the incorporation of GP hydrogel into the P-60HA scaffold enhanced ALP activity, which was ≈4.57 times (****$p < 0.0001$) higher than P-0HA at day 21.

The expression levels of osteogenesis markers were analyzed by real-time reverse quantitative PCR (RT-qPCR), and each value was normalized to day 0 of P-0HA scaffold for comparison between groups (Fig. 3E). The results showed that P-60HA/GP upregulated early (Runt-related transcription factor 2, RUNX2) (≈5-fold) and intermediate (Osteopontin, OPN) markers (≈39-fold) compared to P-0HA from the early time point, day 7. By day 14, while the trend in OPN levels differed in P-60HA/GP from the other scaffolds, it maintained 5- and 1.5-fold higher levels than those of P-0HA and P-60HA, respectively. The late-stage marker, osteocalcin (OCN), exhibited upregulation at day 14 in both P-60HA and P-60HA/GP, with the P-60HA/GP showing enhanced levels 1.7 times compared to P-0HA.

Taken together, P-60HA/GP induced early osteogenesis with high levels of ALP activity, RUNX2, and OPN during the proliferative phase before mineralization and upregulated OCN promoting apatite mineralization *in vitro* [50].

2.4. P-60HA/GP exhibits favorable tissue interaction and biocompatibility in vivo

We investigated the immune response and tissue interaction associated with P-HA scaffolds through subcutaneous implantation in a mouse model (Fig. 4A). After biomaterial implantation, an initial acute inflammation typically initiates within a week, followed by a chronic inflammatory response [51,52]. To examine the relative short-term and long-term immune responses between groups, we established two experimental time points at 7 and 35 days, respectively. The infiltration of cells within the scaffold serves as an indicator of the scaffold's capability to facilitate cell attachment, proliferation, and migration within its structure [53]. H&E staining results (Fig. 4B) revealed mild connective tissue and cellular infiltration into the porous scaffold structure by day 7 in all experimental groups, and there were no significant inflammatory responses at the implantation site. Notably,

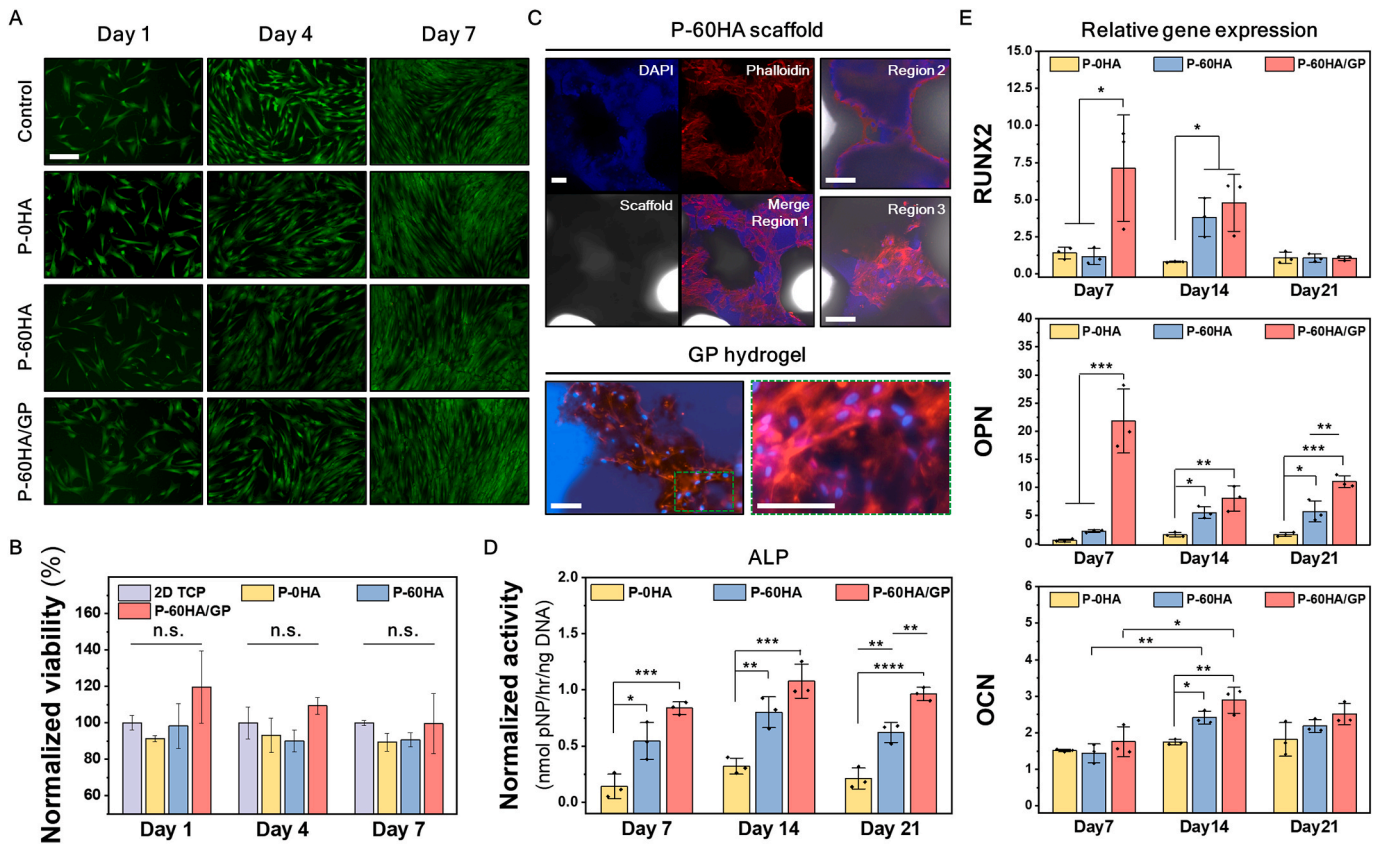

Fig. 3. *In vitro* assessment of cell viability and osteogenic differentiation of hMSCs on the scaffolds. (**A**) Live/dead staining images of each group on days 1, 4, and 7 days. Scale bar, 200 μm. (**B**) Cell viability in the alamarBlue assay normalized to the TCP control group. n.s.: no significant difference; Error bars, ±SD; n = 3. (**C**) Cytoskeleton staining images of hMSCs on P-60HA scaffold and GP hydrogel in P-60HA/GP scaffold 4 days after cell seeding. Scale bars, 100 μm. (**D**) ALP activity normalized to DNA concentration in each group on days 7, 14, and 21. $^{*}p < 0.05$, $^{**}p < 0.01$, $^{***}p < 0.001$ and $^{****}p < 0.0001$; Error bars, ±SD; n = 3. (**E**) The relative expression levels of RUNX2, OPN, and OCN for hMSCs cultured in each group at days 7, 14, and 21. All expression levels were quantified using $2^{-\Delta\Delta CT}$ method and then normalized to the value of the housekeeping gene GAPDH and day 0 for the P-0HA group. $^{*}p < 0.05$, $^{**}p < 0.01$, $^{***}p < 0.001$ and $^{****}p < 0.0001$; Error bars, ±SD; n = 3.

P-60HA/GP exhibited robust cell infiltration at the administered GP hydrogel area. This cell recruitment can be attributed to the favorable effects of the gelatin [23,54,55] and GO components [26] in the GP hydrogel. By day 35, all scaffolds demonstrated successful integration with the surrounding tissue network, and some biomaterial-associated multinucleated giant cells (BMGCs) were observed around the surface of the scaffolds. These cells are typically observed in response to foreign body reactions of polymeric implants [49,56]. BMGCs may act as key regulators during biomaterial integration and have the potential to contribute to the vascularization of the implant bed, ultimately stimulating bone formation [56]. This observation suggests that P-HA scaffolds interact with surrounding tissues and induce cellular responses, contributing to tissue remodeling.

At 35 days, Masson's trichrome staining (Fig. 4C) was performed to assess the capacity to facilitate effective integration with adjacent tissues and act as a substrate for the deposition of new ECM. All P-HA scaffolds exhibited collagen fibril formation throughout their porous structures. Specifically, within the P-60HA/GP scaffold, there was observable tissue infiltration aligned along the site of GP hydrogel injection. This observation is attributed to the interaction between GO and collagen fibers [27], such as hydrogen bonding, electrostatic interaction, and π-π stacking [57,58]. The stable ECM network formation surrounding the scaffolds and within their structure was also confirmed in SEM (Fig. 4D). Overall, these results showed the potential of P-HA scaffolds and GP hydrogel to stimulate cell and tissue ingrowth over time, indicating their suitability as an implant for tissue reconstruction.

2.5. GP hydrogel affects angiogenesis and M2 macrophage polarization

Timely vascularization supplies oxygen and nutrients during bone repair, thereby enhancing bone formation [59]. To further evaluate their potential in stimulating angiogenesis, we conducted immunofluorescence (IF) analysis on the tissue formed within the porous structure of the scaffolds (n = 6 from three biologically independent mice) (Fig. 4E). The newly formed blood vessels displayed α-SMA expression on their outer diameter and CD31 on their inner diameter, and angiogenesis was quantified by evaluating tissue where both markers were co-expressed. At 35 days post-implantation, there was no statistically significant difference ($p = 0.17$) observed between P-0HA (10 ± 3 vessels/mm^2) and P-60HA (15 ± 3 vessels/mm^2) as delineated by CD31 and α-smooth muscle actin (α-SMA) markers (Fig. 4F). However, P-60HA/GP demonstrated enhanced blood vessel formation (18 ± 3 vessels/mm^2) ($^{**}p < 0.01$) compared to the P-0HA, suggesting that the inclusion of GP hydrogel accelerates angiogenesis [60,61].

Once the biomaterial is implanted, an inflammatory reaction is observed typical of foreign body response [62]. Macrophages are one of the first cells to encounter the implanted materials and the major modulator of tissue integration [63], and they exhibit a wide range of capabilities, capable of transitioning from an M1 type (pro-inflammatory state) to an M2 type (anti-inflammatory state) [64]. During the bone regeneration period, the long-term M1 macrophage environment after implantation may lead to bone destruction, hindering the process of bone regeneration and repair. We evaluated the degree of inflammation and macrophage polarization using IF staining with F4/80

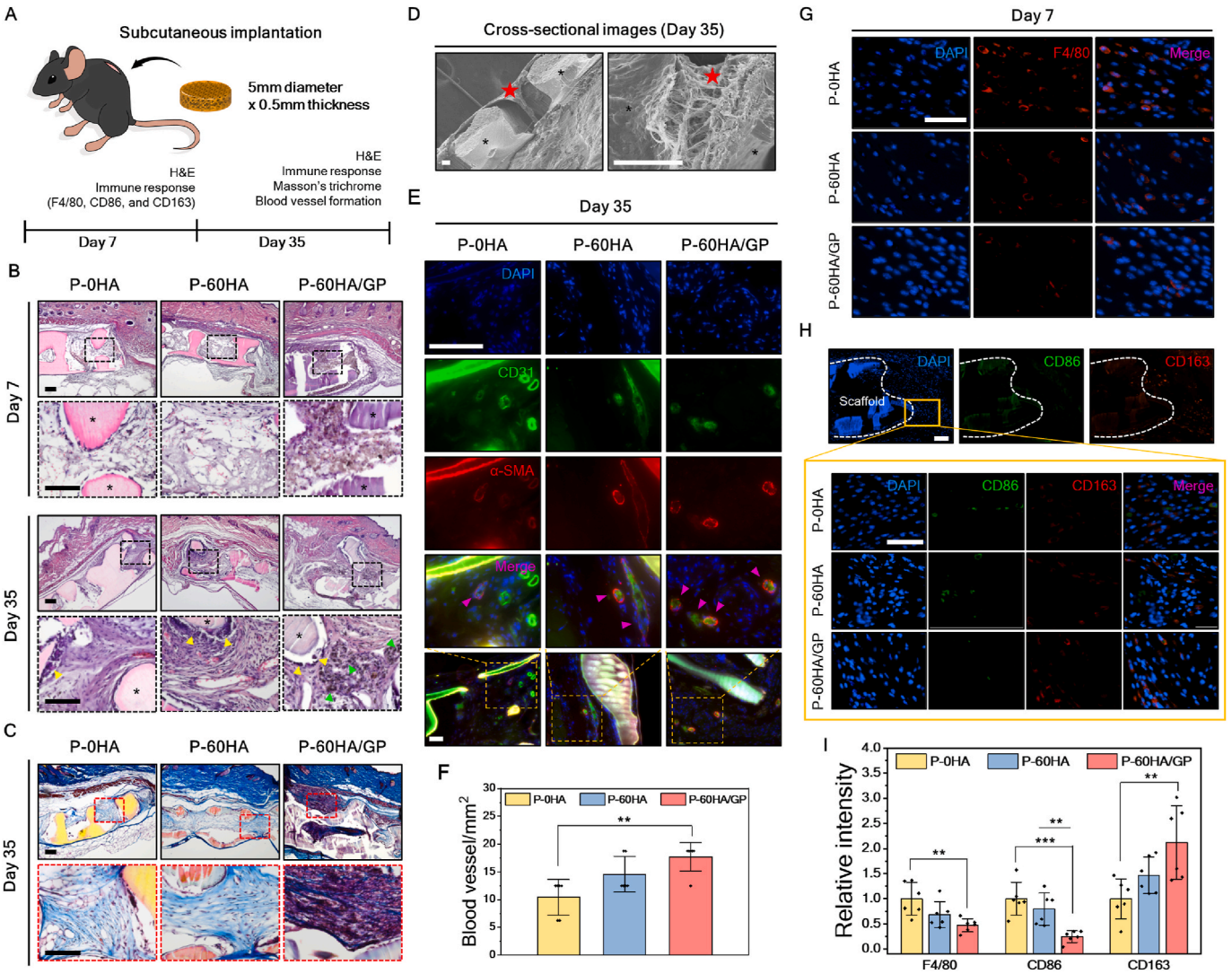

Fig. 4. Evaluation of *in vivo* immune response and biocompatibility of scaffolds in mouse subcutaneous implantation. (**A**) Schematic illustration of the subcutaneous implantation experiment. (**B**) Cross-sectional H&E histological images of scaffold implanted tissue at day 7 and day 35. The images at the bottom represent the higher magnification of each group. The asterisk (*): scaffold; Green arrowhead: GO residue; Yellow arrowhead: multinucleated giant cells. Scale bars, 150 μm. (**C**) Representative Masson's trichrome staining images at day 35 after implantation and their higher magnification images. The asterisk (*), scaffold; Scale bars, 50 μm. (**D**) Cross-sectional SEM images of the implanted scaffold on day 35. The asterisk (*): scaffold; Star: infiltrated tissues. Left: under 100X magnification; Right: 1,000× magnification. Scale bars, 50 μm. (**E**) Representative immunofluorescence staining images of CD31 and α-SMA on day 35. Pink arrowhead: newly formed blood vessel. Scale bar, 100 μm. (**F**) The quantitative analysis of blood vessel formation inside scaffolds on day 35. $^{**}p < 0.01$, Error bars, ±SD; n = 6. (**G**) Representative immunofluorescence staining images of F4/80, (**H**) CD86, and CD163 markers on day 7. Scale bars, 50 μm. (**I**) The relative quantitative mean gray value of F4/80, CD86, and CD163 on day 7. $^{**}p < 0.01$, and $^{***}p < 0.001$, Error bars, ±SD; n = 6.

(pan macrophages), CD86 (M1 macrophages), and CD163 (M2 macrophages) (n = 6 from three biologically independent mice) (Fig. 4G and H). The analysis was performed on the adjacent tissues surrounding the implanted scaffold, and the relative mean gray value was determined based on the P-0HA value at day 7 (Fig. 4I). At 35 days, F4/80 and CD86 levels were decreased in all groups (mean value < 0.5) (Fig. S8) by the transition from the pro-inflammatory to anti-inflammatory phase, and there was no significant difference between groups ($p > 0.05$). However, on day 7, P-60HA/GP showed low F4/80 intensity (0.5 ± 0.1) and significantly reduced CD86 levels (0.2 ± 0.1) (Fig. 4I). In particular, P-60HA/GP showed a higher M2 macrophage expression (2.1 ± 0.7) and M2 polarization (Fig. S9).

2.6. P-60HA/GP accelerates bone formation in critical-sized cranial defects

We evaluated the *in vivo* osteogenic capabilities of P-HA scaffolds using a mouse calvarial defect model (Fig. 5A). The scaffolds were printed to match the bone defects (4mm × 0.3 mm) (Fig. S10), and the new bone formation was monitored by micro-computed tomography (μCT) scanning until 12 weeks (Fig. 5B). Despite the similar HA content between P-60HA (594.8 mg HA/cm^3) and native bone (710.159 mg HA/cm^3) (Fig. S11), the newly formed tissue exhibits a relatively low mineral content and density. This difference allows the new tissue to be visualized within the low threshold range (Figs. S12 and S13). We segmented the area into two regions to facilitate visualization and quantification of bone formation following the regeneration process (n = 5 for scaffold groups and n = 3 for blank). According to the threshold ranges, tissue formations, including the P-60HA scaffold, were highlighted in green and yellow on the μCT images (Fig. 5B) and categorized as low-density and high-density immature bone, respectively (Fig. 5C and D). In the lower threshold range (140–300 mg HA/cm^3), the scaffold and soft tissue (brain, scalp, and fat) were disregarded from visualization (Fig. S12), allowing focus solely on the tissues infiltrated at the

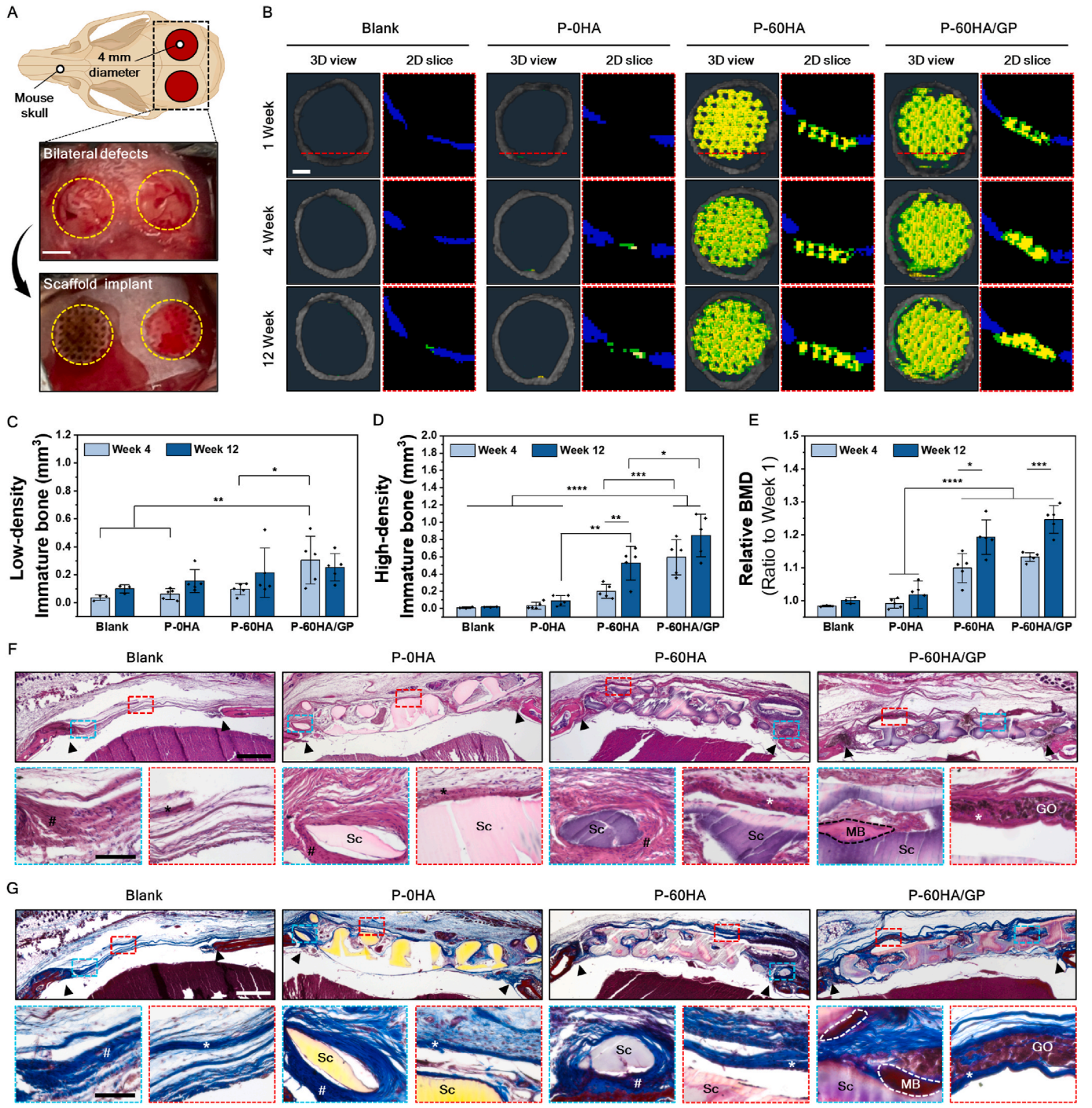

Fig. 5. Bone reconstruction by scaffolds in murine critical-sized cranial defect model. (**A**) Schematic illustration and photos of *in vivo* cranial defect repair experiment. Scale bar, 2 mm. (**B**) Representative micro-CT images at 1, 4, and 12 weeks. Blank: no treatment; Green: tissues and scaffolds in the low threshold range; Yellow: tissues and scaffolds in the high threshold range. Scale bar, 1 mm. (**C and D**) Quantitative analyses of immature bone formation in each group at 4 and 12 weeks compared to at 1 week, and (**E**) relative BMD of each group. $^{*}p < 0.05$, $^{**}p < 0.01$, $^{***}p < 0.001$ and $^{****}p < 0.0001$; Error bars, ±SD; n = 5. (**F**) H&E staining and (**G**) Masson's trichrome staining of each group at 12 weeks after implantation. Scale bars, 500 μm. The images at the bottom represent the higher magnification of each area. Scale bars, 100 μm. Red dash: around the edge; Blue dash: around the center; Sc: scaffold; Black arrow: defect area; Hash (#): unmineralized osteoid; The asterisk (*): periosteal layer; MB: mature bone fragment; GO: GO residue.

peripheral border and voids of the scaffold. The bone reconstruction process involves infiltration of an ECM network, including the formation of collagen fibrils, followed by mineralization by osteoblasts to create mechanically stable bone in the form of lamellae [65]. Therefore, the lower threshold range involves the low-density immature bone, including the collagen network and ECM [65]. The progression of tissue growth and maturation into the high-density threshold range is supported by μCT scanning results taken over time (Fig. S13). On the other hand, the higher global threshold range (above 300 mg HA/cm^3) was utilized to evaluate the high-density immature bone, which includes the P-60HA scaffold, unmineralized osteoid, and mineralized tissues.

The volume of newly formed tissue in the defect area was quantified based on week 1 of each group. P-60HA/GP showed a considerable low-density immature bone formation (0.3 ± 0.2 mm^3) at an early stage

(week 4), exhibiting an 8.4-fold increase compared to the blank (0.04 ± 0.02 mm^3) (**$p < 0.01$) (Fig. 5C). This observation suggests that during the early stage, the presence of GP hydrogel facilitated the development of dense collagen fibers and the formation of ECM found surrounding the scaffold. At 12 weeks, certain experimental groups of P-60HA/GP exhibited a relatively decreased formation compared to week 4. This result indicates maturation in tissue formation due to collagen fiber crosslinking [65], transitioning towards the stage of high-density immature bone (Fig. S13). It suggests the predominant formation of high-density bone (above 75 %) at 12 weeks (Fig. S14). Furthermore, within 4 weeks, P-60HA/GP significantly promoted mature bone formation (0.6 ± 0.2 mm^3), exceeding the blank (0.009 ± 0.01 mm^3) (****$p < 0.0001$) by 69 times and P-60HA (0.2 ± 0.1 mm^3) (***$p < 0.001$) by 3 times (Fig. 5D). At 4 weeks, both P-60HA and P-60HA/GP showed increased bone mineral density compared to P-0HA (Fig. 5E), which was attributed to HA elevating local Ca^{2+} concentrations [66,67]. However, at 12 weeks, P-60HA/GP exhibited significant enhancement (***$p < 0.001$) compared to the increase in P-60HA (*$p < 0.05$), representing 1.24 times increase compared to week 1 (Fig. 5E and Fig. S11C).

At 12 weeks, the tissues from the center of the defect area were sectioned and examined for analysis. H&E and Masson's trichrome staining (Fig. 5F and G) showed that P-60HA/GP induced mature new bone fragments between pores and around the structure, while other scaffolds resulted in unmineralized osteoid at the boundary of the defect area. Compared to week 4 (Fig. S15), minimal GO residual was observed in the P-60HA/GP implanted group, suggesting gradual *in vivo* degradation of GO [68]. Moreover, at week 4, P-60HA/GP supported connective tissue formation throughout its structure and showed relatively high M2 macrophage polarization (Fig. S16). While no significant difference was observed in the pro-inflammatory macrophage phenotype and cytokine levels at each time point (Fig. S16 and Fig. S17),

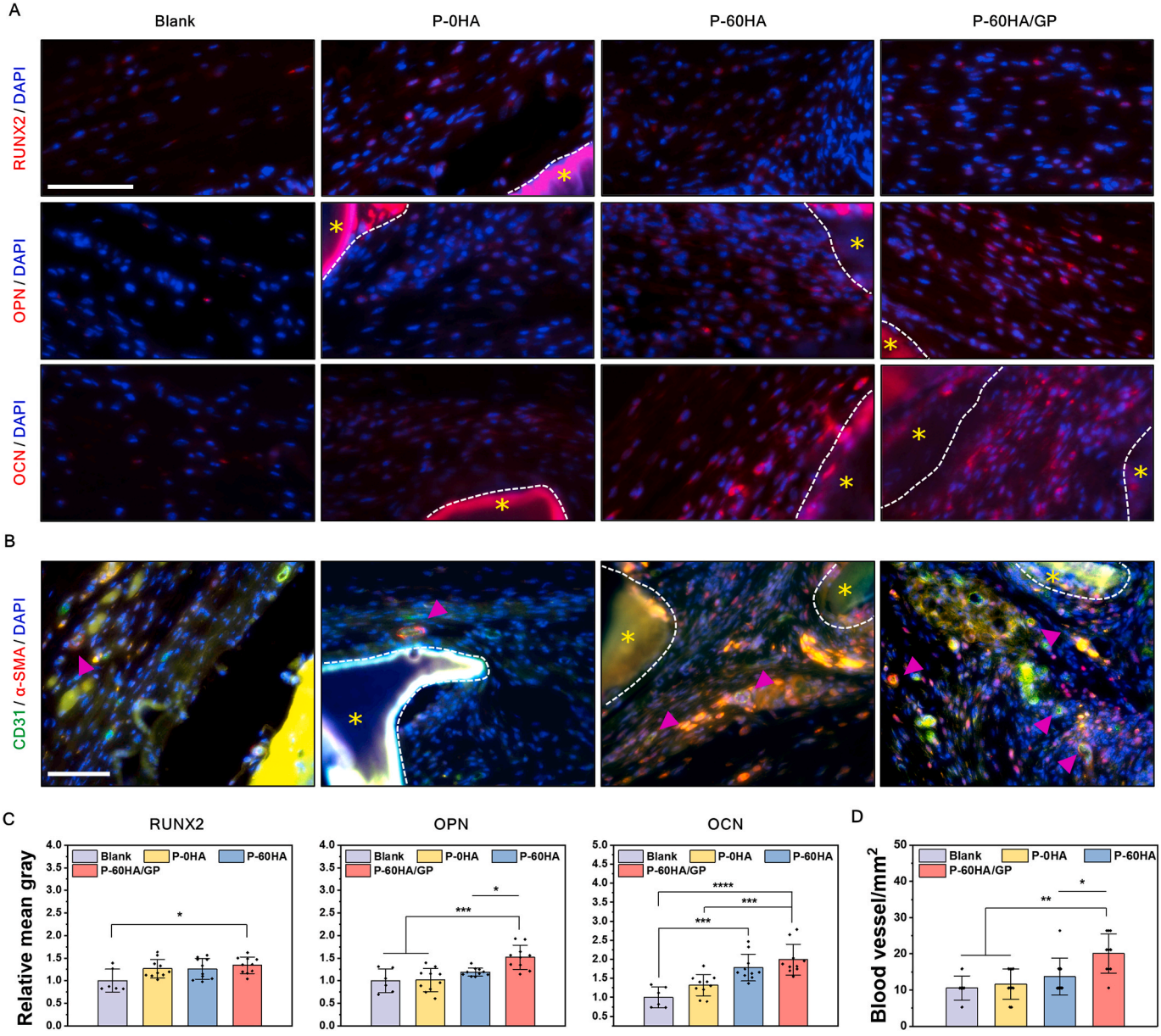

Fig. 6. Osteogenic potential and angiogenesis assessments of scaffolds in cranial defect model. (**A**) Representative immunofluorescence staining images of osteogenic markers and (**B**) CD31, and α-SMA markers on each scaffold after 12 weeks of implantation. The asterisk (*): scaffold; Pink arrow: newly formed blood vessel. Scale bar, 100 μm. (**C**) Relative mean gray value of each osteogenic differentiation markers on different groups, and (**D**) the quantitative analysis of blood vessel formation. *$p < 0.05$, **$p < 0.01$, ***$p < 0.001$ and ****$p < 0.0001$; Error bars, ±SD; n = 10.

P-60HA/GP exhibited a notable increase in anti-inflammatory expression.

Effective reconstruction of the periosteal layer is crucial to promote bone formation, given its ability to supply abundant growth factors for bone cell growth and differentiation [69–71]. P-60HA and P-60HA/GP induced rich periosteal layers around their structure, while the blank and P-0HA formed less connective collagen structures (Fig. 5G). Interestingly, collagen fibers were formed along injected GP hydrogel in the P-60HA/GP scaffold, which aligned with the findings from the subcutaneous implantation model (Fig. 4C). This outcome demonstrated that P-60HA/GP facilitated the development of aligned collagen formation, which favored bone tissue growth [69].

2.7. P-60HA/GP promotes the osteogenesis of endogenous cells and angiogenesis

At week 12, the osteogenic and angiogenic capacity were assessed through IF staining with osteogenic markers (RUNX2, OPN, and OCN) and CD31/α-SMA (Fig. 6A and B). The osteogenic markers were labeled with a red fluorescent dye, and their intensity (n = 10 from five biologically independent mice) was evaluated relative to the mean gray value of the blank (n = 6 from three biologically independent mice) at week 12 (Fig. 6C).

The quantitative results of RUNX2 indicated high expression levels and significant improvements in P-60HA/GP from week 4 (1.5 ± 0.2) (***$p < 0.001$) (Fig. S18) to week 12 (1.3 ± 0.2) (*$p < 0.05$) compared to the blank, while the other groups exhibited no significant differences ($p > 0.05$) from the blank at week 12 (Fig. 6C). Furthermore, P-60HA/GP showed strong signal intensities in both OPN (1.5 ± 0.3) (***$p < 0.001$) and OCN (2 ± 0.4) (****$p < 0.0001$) compared to those of the blank, which were observed from the early stage (Fig. S18). These findings suggest that P-60HA/GP promotes pre-osteoblast proliferation and maturation, thereby facilitating mineralization [50].

Significant outcomes were also found in angiogenesis (Fig. 6, B and D). While the P-60HA resulted in slightly higher blood vessel formation (14 ± 5 vessels/mm^2) compared to the blank (11 ± 3 vessels/mm^2) and P-0HA (12 ± 4 vessels/mm^2) groups, this difference was not statistically significant ($p > 0.05$). In contrast, P-60HA/GP exhibited a progressive

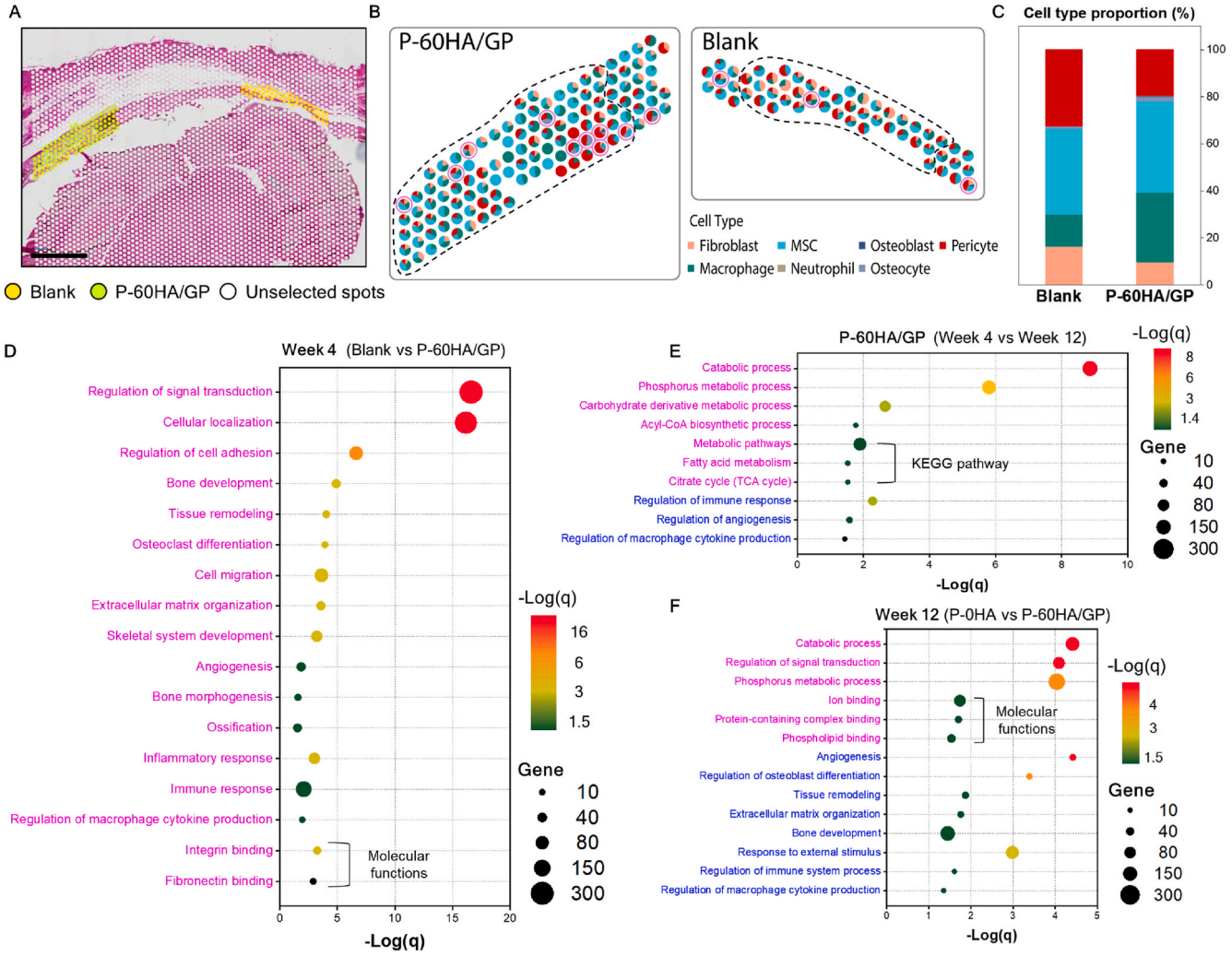

Fig. 7. Spatial transcriptomics evaluation of cell and tissue responses to calvarial bone defects treated with and without scaffolds. (**A**) Region of interest capture location in an H&E-stained tissue section. Scale bar, 2 mm. (**B**) Deconvoluted cell types assigned to each capture location and (**C**) the overall cell type proportions in each region of interest. Pink circles: capture locations with osteoblasts and osteocytes; Black dash: newly formed tissue area 0.45 mm from the surrounding bone (middle of defect area). (**D**) Dot plot of gene ontology biological processes and molecular functions for the differentially expressed genes (DEGs) upregulated in P-60HA/GP compared to Blank at 4 weeks. (**E**) Gene ontology biological processes and KEGG pathway analyses for DEGs in P-60HA/GP at 12 weeks compared to 4 weeks and (**F**) P-0HA at 12 weeks. Pink: pathways based on the upregulated (log2FC > 1) DEGs; Blue: pathways based on the downregulated (log2FC < −1) DEGs. DEGs (log2FC > 1 and log2FC < −1) from pairwise comparisons were used to determine gene ontology and KEGG pathway analysis using DAVID tool. The p-values were adjusted using the Benjamini–Hochberg method, and adjusted p-value (q-value) <0.05 was selected as the cutoff to identify the significantly enriched terms.

vessel formation (20 ± 5 vessels/mm^2) (**$p < 0.01$ for the blank and P-0HA; *$p < 0.05$ for P-60HA), particularly pronounced starting from week 4 (12 ± 4 vessels/mm^2) (Fig. S19).

2.8. P-60HA/GP recruits few fibroblasts and numerous macrophages

Based on the significant differences observed at 4 weeks (Fig. 5), spatial transcriptomics was performed to elucidate the mechanism of P-60HA/GP on early bone tissue formation. Comparisons were made under identical biological conditions, and after quality control, 351 (Blank) and 252 (P-60HA/GP) unique genes in the capture location were included in the analysis (Fig. 7A and Table S2). We deconvoluted the capture location into specific cell types (Fig. 7B) and estimated their proportions (Fig. 7C). P-60HA/GP exhibited a low proportion of osteocytes and osteoblasts (1.96 %) yet intriguingly occupied the central defect area, whereas, in the blank, these cells were mainly near the surrounding native bone (0.69 %) (Fig. 7B). Given the limited presence of osteoblasts within the defect and the necessity to recruit endogenous cells from surrounding tissues for complete osseointegration [72], our findings indicate that P-60HA/GP facilitated the recruitment and differentiation of progenitor cells.

Compared to the blank, P-60HA/GP showed significantly lower proportions of fibroblasts (9.9 %) (Blank: 17.6 %) and pericytes (19.5 %) (Blank: 26.4 %), as well as a significantly higher proportion of macrophages (29.6 %) (Blank: 19.4 %) (Fig. 7C and Table S3). The sparse and scattered distribution of fibroblasts in P-60HA/GP suggests minimal fibrosis around the scaffold [73], with numerous macrophages attributed to the biological response of the immune system for the implant [51].

2.9. P-60HA/GP upregulates genes involved in immune and metabolic processes

To uncover the biological pathways underlying the differential cell type distribution in P-60HA/GP, we performed gene ontology enrichment analysis on differentially expressed genes (DEGs) (Table S4). Compared to the blank at 4 weeks, P-60HA/GP enriched processes associated with immune and inflammatory responses and macrophage cytokine production along with tissue remodeling, bone morphogenesis, and ossification (Fig. 7D). In addition, genes associated with molecular functions such as integrin and fibronectin bindings were over-represented (adjusted $p < 0.001$) (Fig. 7D), indicating the enhanced cell adhesion properties of the GP hydrogel [23,26,27]. Specifically, despite a low proportion of pericytes in P-60HA/GP (Fig. 7C), it upregulated processes related to angiogenesis. Fibroblasts share some markers with mural cells, posing challenges in distinguishing gene profiles between pericytes and perivascular fibroblasts, forming the fibrotic scar [74,75]. The excessive presence of these cell types in the blank suggests fibrotic scarring.

At 12 weeks, P-60HA/GP showed prominent enrichment in biological processes and KEGG pathways related to the metabolic processes when compared to the early time point (Fig. 7E). Notably, genes linked to the regulation of immune response, angiogenesis, and cytokine production were downregulated. A similar pattern was also observed in comparison with P-0HA at 12 weeks (Fig. 7F). Although there were no significant differences in cell type proportions between P-0HA and P-60HA/GP (Fig. S20 and Table S3), genes involved in tissue regeneration and immunity were downregulated, while metabolic processes were upregulated.

Overall, the high macrophage proportion in P-60HA/GP suggests a significant role in both immune and metabolic processes. Pathway analyses highlight the interdependent relationship between the immune response, tissue development, and angiogenesis in the early osseointegration process. Our transcriptomic analyses align with the histological data (Fig. S16), demonstrating M2 polarity in the P-60HA/GP group. In the later stages of bone healing in P-60HA/GP, macrophages are primarily involved in catabolic and metabolic processes, contributing to secondary bone formation [76].

3. Discussion

Meeting the global demand for simple and scalable regenerative biomaterials while complying with clinical standards and minimizing cost remains a significant challenge [77]. The 3D-printed porous CSS presented herein provides a rigid (P-60HA)-soft (GP hydrogel) hybrid microenvironment that mimics natural bone [78]. The fabrication of this hybrid CSS is simple and scalable for manufacturing while meeting the conformal requirements to reconstruct craniofacial defects [10,79,80]. From a clinical standpoint, we provide the benefits of expedited treatment applications even for critical-sized defects. Citrate plays a crucial role as a bioactive factor in bone [81]. Both mPOC and PPCN, integral components of the CSS, are polymers that belong to a biomaterial technology referred to as citrate-based biomaterials (CBB) [22,34]. A CBB, referred to as CITREGEN, has been used to fabricate biodegradable implantable medical devices that have been cleared by the U.S. Food and Drug Administration (FDA) to attach soft tissue to bone [22]. Therefore, given that the FDA is familiar with this new composition and class of polymers (biodegradable thermosets), the CSS is primed for translational application.

Importantly, our strategy eliminates dependence on exogenous biological factors and demonstrates proficient tissue integration and osteogenic potential solely through material-driven cues. The viscoelastic environment of GP hydrogel with rapid stress relaxation (Fig. 2F) promotes intracellular response and tissue remodeling [46,48]. Additionally, gelatin and GO components reinforce cell adhesion [46,82,83], and GO synergizes with HA [28,29] in mineralization and enhancing bone formation [84,85]. Spatial transcriptomics (Fig. 7) suggest that P-60HA/GP promotes osseointegration by enhancing molecular functions and biological processes related to protein binding, cell migration, cell adhesion, and ECM organization by week 4 (Fig. 7C and D). Moreover, upregulated genes associated with ossification and bone morphogenesis in the first 4 weeks confirm the osteoinductive properties of P-60HA/GP.

We observed notable differences in macrophage proportions and immune system activity in defects treated with P-60HA/GP (Fig. 7). The interplay between macrophage metabolism and various metabolic pathways is critical for bone healing and tissue regeneration [86]. During bone remodeling, MSCs utilize various metabolic pathways to acquire the energy required for differentiation and function, with a notable increase in mitochondrial metabolism [87]. Specifically, osteoblasts need ATP to enhance mineralization [88], and the citrate cycle (TCA cycle) produces substantial ATP with oxidative phosphorylation, which is utilized for both osteoblasts and osteoclasts during the osteogenic program [76]. Following tissue injury, M2 macrophages promote tissue remodeling through upregulation of the TCA cycle and mitochondrial metabolism, which remain active during tissue regeneration [89,90]. Citrate, a metabolite in the TCA cycle, also plays critical roles in both M1 and M2 macrophage activities [30].

M2 macrophages play a crucial role in alleviating inflammation and regulating angiogenesis and tissue repair [64]. The initial high macrophage proportions and immune response in P-60HA/GP correlate with our histological findings (Figs. S16 and S17). The high M2 polarization in defects treated with P-60HA/GP is expected to have promoted angiogenesis, facilitating prompt tissue integration and osseointegration [86]. The subsequent reduction in the immune response can be attributed to the antioxidant properties inherent in citrate [30,33], and citrate accumulation in mitochondria exerting indirect anti-inflammatory effect [30]. In other words, at 12 weeks, macrophages primarily contribute to metabolic processes, and upregulated activity of the TCA cycle and metabolism involving phosphorus, lipids, and acyl-CoA appear to play a prominent role in a late phase of bone healing and maturation [86].

While spatial transcriptomics revealed the potential effect of GP hydrogel on bone regeneration by comparing them with the blank and P-0HA at protein and gene levels, a direct comparison with P-60HA at the gene level is lacking. We believe this gap can be addressed through *in vitro* assessment, μCT quantification, and histological analysis. Also, previous studies show that the integration of HA and GO enhances osteogenic differentiation compared to their individual use [84].

Previous studies demonstrated dose-dependent toxicity of GO through intravenous injection in mice [91]. A dosage of 0.25 mg per mouse from these studies was not toxic or lethal. We administered a 16.5 μg GO dose (0.33 mg/mL in 50 μL GP hydrogel) within the acceptable tolerance range established by previous studies [91]. While we demonstrated the potential degradability of GO during *in vivo* bone healing, its long-term effects until complete bone healing are not known.

Our results have not been directly compared to autologous grafts or systems integrating exogenous cells and growth factors. Our primary focus has been on effective bone and tissue reconstruction while minimizing costs, procedures, and potential immune responses, all geared toward swift translation and clinical implementation. Future work will involve evaluating our CSS in larger animals.

Ethics approval and consent to participate

The mouse subcutaneous implantation model was carried out with the approval from the Institutional Animal Care and Use Committee at Northwestern University (protocol #IS00003238). The cranial defect animal procedure was performed in compliance with the approval from the University of Chicago Animal Care and Use Committee (ACUP #71745).

Data and materials availability

All data is available in the main text or the supplementary materials.

Funding

This work was supported by the National Research Foundation of Korea (2021R1A6A3A14039205) (Mirae Kim); the National Institutes of Health/National Institute of Dental and Craniofacial Research (R01DE030480) (Russell R. Reid).

Ethics approval and consent to participate

The mouse subcutaneous implantation model was carried out with the approval from the Institutional Animal Care and Use Committee at Northwestern University (protocol #IS00003238). The cranial defect animal procedure was performed in compliance with the approval from the University of Chicago Animal Care and Use Committee (ACUP #71745).

CRediT authorship contribution statement

Mirae Kim: Writing – review & editing, Writing – original draft, Visualization, Methodology, Investigation, Conceptualization. **Xinlong Wang:** Methodology, Investigation. **Yiming Li:** Formal analysis, Visualization. **Zitong Lin:** Formal analysis, Visualization. **Caralyn P. Collins:** Writing – review & editing, Visualization, Methodology, Investigation. **Yugang Liu:** Methodology, Investigation. **Yujin Ahn:** Visualization, Methodology, Investigation. **Hsiu-Ming Tsal:** Visualization, Methodology, Investigation. **Joseph W. Song:** Methodology, Investigation. **Chongwen Duan:** Methodology, Investigation. **Yi Zhu:** Investigation. **Cheng Sun:** Methodology. **Tong-Chuan He:** Writing – review & editing, Methodology. **Yuan Luo:** Data curation, Formal analysis, Visualization. **Russell R. Reid:** Writing – review & editing, Supervision, Investigation, Conceptualization. **Guillermo A. Ameer:** Writing – review & editing, Supervision, Conceptualization.

Declaration of competing interest

None

Acknowledgments

We extend special thanks to Piao Zhao, Guozhi Zhao, and Yonghui Wang from The University of Chicago Medical Center. This work was supported by the Northwestern University NUSeq Core Facility, and made use of the IMSERC NMR and Physical Characterization facility at Northwestern University, which has received support from the Soft and Hybrid Nanotechnology Experimental (SHyNE) Resource (NSF ECCS-2025633), and Northwestern University. This work made use of the Keck-II facility and the EPIC facility of Northwestern University's NUANCE Center, which has received support from the SHyNE Resource (NSF ECCS-2025633), the IIN, and Northwestern's MRSEC program (NSF DMR-2308691). Imaging work was performed at the Northwestern University Center for Advanced Molecular Imaging (RRID:SCR_021192) generously supported by NCI CCSG P30 CA060553 awarded to the Robert H Lurie Comprehensive Cancer Center.

Appendix A. Supplementary data

Supplementary data to this article can be found online at https://doi.org/10.1016/j.bioactmat.2024.07.029.

References

[1] L.A. Kandi, T.L. Jarvis, M. Shrout, D.A. Thornburg, M.A. Howard, M. Ellis, C. M. Teven, Trends in medicare reimbursement for the top 20 surgical procedures in craniofacial trauma, J. Craniofac. Surg. 34 (2023) 247–249.
[2] M.J. Carty, N. Ferraro, J. Upton, Reconstruction of pediatric cranial base defects: a review of a single microsurgeon's 30-year experience, J. Craniofac. Surg. 20 (2009) 639–645.
[3] S. Bhumiratana, J.C. Bernhard, D.M. Alfi, K. Yeager, R.E. Eton, J. Bova, F. Shah, J. M. Gimble, M.J. Lopez, S.B. Eisig, Tissue-engineered autologous grafts for facial bone reconstruction, Sci. Transl. Med. 8 (2016), 343ra383-343ra383.
[4] T.W. Bauer, G.F. Muschler, Bone graft materials: an overview of the basic science, Clin. Orthop. Relat. Res. 371 (2000) 10–27.
[5] G.L. Koons, M. Diba, A.G. Mikos, Materials design for bone-tissue engineering, Nat. Rev. Mater. 5 (2020) 584–603.
[6] N.L. Hunter, R.E. Sherman, Combination products: modernizing the regulatory paradigm, Nat. Rev. Drug Discov. 16 (2017) 513–514.
[7] A. De Pieri, Y. Rochev, D.I. Zeugolis, Scaffold-free cell-based tissue engineering therapies: advances, shortfalls and forecast, NPJ Regenerative Medicine 6 (2021) 18.
[8] F. Shang, Y. Yu, S. Liu, L. Ming, Y. Zhang, Z. Zhou, J. Zhao, Y. Jin, Advancing application of mesenchymal stem cell-based bone tissue regeneration, Bioact. Mater. 6 (2021) 666–683.
[9] J.A. Burdick, R.L. Mauck, J.H. Gorman III, R.C. Gorman, Acellular biomaterials: an evolving alternative to cell-based therapies, Sci. Transl. Med. 5 (2013), 176ps174-176ps174.
[10] J.R. Tumbleston, D. Shirvanyants, N. Ermoshkin, R. Janusziewicz, A.R. Johnson, D. Kelly, K. Chen, R. Pinschmidt, J.P. Rolland, A. Ermoshkin, Continuous liquid interface production of 3D objects, Science 347 (2015) 1349–1352.
[11] R.L. Keate, J. Tropp, C.P. Collins, H.O.T. Ware, A.J. Petty, G.A. Ameer, C. Sun, J. Rivnay, 3D-Printed electroactive hydrogel architectures with sub-100 μm resolution promote myoblast viability, Macromol. Biosci. 22 (2022) 2200103.
[12] X. Gui, B. Zhang, Z. Su, Z. Zhou, Z. Dong, P. Feng, C. Fan, M. Liu, Q. Kong, C. Zhou, 3D-printed degradable hydroxyapatite bioactive ceramics for skull regeneration, MedComm–Biomaterials and Applications 2 (2023) e41.
[13] S.R. Shah, S. Young, J.L. Goldman, J.A. Jansen, M.E. Wong, A.G. Mikos, A composite critical-size rabbit mandibular defect for evaluation of craniofacial tissue regeneration, Nat. Protoc. 11 (2016) 1989–2009.
[14] H.E. Talbott, S. Mascharak, M. Griffin, D.C. Wan, M.T. Longaker, Wound healing, fibroblast heterogeneity, and fibrosis, Cell Stem Cell 29 (2022) 1161–1180.
[15] A. Atala, F.K. Kasper, A.G. Mikos, Engineering complex tissues, Sci. Transl. Med. 4 (2012), 160rv112-160rv112.
[16] L. Nie, Y. Deng, P. Li, R. Hou, A. Shavandi, S. Yang, Hydroxyethyl chitosan-reinforced polyvinyl alcohol/biphasic calcium phosphate hydrogels for bone regeneration, ACS Omega 5 (2020) 10948–10957.
[17] K. Zhou, P. Yu, X. Shi, T. Ling, W. Zeng, A. Chen, W. Yang, Z. Zhou, Hierarchically porous hydroxyapatite hybrid scaffold incorporated with reduced graphene oxide for rapid bone ingrowth and repair, ACS Nano 13 (2019) 9595–9606.
[18] Z. Zhong, X. Wu, Y. Wang, M. Li, Y. Li, X. Liu, X. Zhang, Z. Lan, J. Wang, Y. Du, Zn/Sr dual ions-collagen co-assembly hydroxyapatite enhances bone regeneration

through procedural osteo-immunomodulation and osteogenesis, Bioact. Mater. 10 (2022) 195–206.
[19] P. Song, M. Li, B. Zhang, X. Gui, Y. Han, L. Wang, W. Zhou, L. Guo, Z. Zhang, Z. Li, DLP fabricating of precision GelMA/HAp porous composite scaffold for bone tissue engineering application, Compos. B Eng. 244 (2022) 110163.
[20] L. Tong, X. Pu, Q. Liu, X. Li, M. Chen, P. Wang, Y. Zou, G. Lu, J. Liang, Y. Fan, Nanostructured 3D-printed hybrid scaffold accelerates bone regeneration by photointegrating nanohydroxyapatite, Adv. Sci. 10 (2023) 2300038.
[21] G. Kaur, V. Kumar, F. Baino, J.C. Mauro, G. Pickrell, I. Evans, O. Bretcanu, Mechanical properties of bioactive glasses, ceramics, glass-ceramics and composites: state-of-the-art review and future challenges, Mater. Sci. Eng. C 104 (2019) 109895.
[22] H. Wang, S. Huddleston, J. Yang, G.A. Ameer, Enabling proregenerative medical devices via citrate-based biomaterials: transitioning from inert to regenerative biomaterials, Adv. Mater. 36 (2024) 2306326.
[23] J. Ye, J. Wang, Y. Zhu, Q. Wei, X. Wang, J. Yang, S. Tang, H. Liu, J. Fan, F. Zhang, A thermoresponsive polydiolcitrate-gelatin scaffold and delivery system mediates effective bone formation from BMP9-transduced mesenchymal stem cells, Biomed. Mater. 11 (2016) 025021.
[24] H.K. Raut, R. Das, Z. Liu, X. Liu, S. Ramakrishna, Biocompatibility of biomaterials for tissue regeneration or replacement, Biotechnol. J. 15 (2020) 2000160.
[25] R.E. McMahon, L. Wang, R. Skoracki, A.B. Mathur, Development of nanomaterials for bone repair and regeneration, J. Biomed. Mater. Res. B Appl. Biomater. 101 (2013) 387–397.
[26] W.C. Lee, C.H.Y. Lim, H. Shi, L.A. Tang, Y. Wang, C.T. Lim, K.P. Loh, Origin of enhanced stem cell growth and differentiation on graphene and graphene oxide, ACS Nano 5 (2011) 7334–7341.
[27] C. Yue, C. Ding, X. Du, Y. Wang, J. Su, B. Cheng, Self-assembly of collagen fibrils on graphene oxide and their hybrid nanocomposite films, Int. J. Biol. Macromol. 193 (2021) 173–182.
[28] C. Santos, C. Piedade, P. Uggowitzer, M. Montemor, M. Carmezim, Parallel nano-assembling of a multifunctional GO/HapNP coating on ultrahigh-purity magnesium for biodegradable implants, Appl. Surf. Sci. 345 (2015) 387–393.
[29] Q. Wang, Y. Chu, J. He, W. Shao, Y. Zhou, K. Qi, L. Wang, S. Cui, A graded graphene oxide-hydroxyapatite/silk fibroin biomimetic scaffold for bone tissue engineering, Mater. Sci. Eng. C 80 (2017) 232–242.
[30] H. Xu, S. Yan, E. Gerhard, D. Xie, X. Liu, B. Zhang, D. Shi, G.A. Ameer, J. Yang, Citric acid: a nexus between cellular mechanisms and biomaterial innovations, Adv. Mater. 2402871 (2024).
[31] J.A. Burke, Y. Zhu, X. Zhang, P.D. Rios, I. Joshi, D. Lopez, H. Nasir, S. Roberts, Q. Rodriguez, J. McGarrigle, Phase-changing citrate macromolecule combats oxidative pancreatic islet damage, enables islet engraftment and function in the omentum, Sci. Adv. 10 (2024) eadk3081.
[32] M. Liu, X. Zeng, C. Ma, H. Yi, Z. Ali, X. Mou, S. Li, Y. Deng, N. He, Injectable hydrogels for cartilage and bone tissue engineering, Bone research 5 (2017) 1–20.
[33] J. Yang, R. Van Lith, K. Baler, R.A. Hoshi, G.A. Ameer, A thermoresponsive biodegradable polymer with intrinsic antioxidant properties, Biomacromolecules 15 (2014) 3942–3952.
[34] J. Yang, A.R. Webb, G.A. Ameer, Novel citric acid-based biodegradable elastomers for tissue engineering, Adv. Mater. 16 (2004) 511–516.
[35] M.M. Hasani-Sadrabadi, P. Sarrion, S. Pouraghaei, Y. Chau, S. Ansari, S. Li, T. Aghaloo, A. Moshaverinia, An engineered cell-laden adhesive hydrogel promotes craniofacial bone tissue regeneration in rats, Sci. Transl. Med. 12 (2020) eaay6853.
[36] H.A. Pearce, J.W. Swain, L.H. Victor, K.J. Hogan, E.Y. Jiang, M.L. Bedell, A. M. Navara, A. Farsheed, Y.S. Kim, J.L. Guo, Thermogelling hydrogel charge and lower critical solution temperature influence cellular infiltration and tissue integration in an ex vivo cartilage explant model, J. Biomed. Mater. Res. 111 (2023) 15–34.
[37] C. Zhao, Z. Zeng, N.T. Qazvini, X. Yu, R. Zhang, S. Yan, Y. Shu, Y. Zhu, C. Duan, E. Bishop, Thermoresponsive citrate-based graphene oxide scaffold enhances bone regeneration from BMP9-stimulated adipose-derived mesenchymal stem cells, ACS Biomater. Sci. Eng. 4 (2018) 2943–2955.
[38] A.L. Olivares, È. Marsal, J.A. Planell, D. Lacroix, Finite element study of scaffold architecture design and culture conditions for tissue engineering, Biomaterials 30 (2009) 6142–6149.
[39] M. Castilho, A. van Mil, M. Maher, C.H. Metz, G. Hochleitner, J. Groll, P. A. Doevendans, K. Ito, J.P. Sluijter, J. Malda, Melt electrowriting allows tailored microstructural and mechanical design of scaffolds to advance functional human myocardial tissue formation, Adv. Funct. Mater. 28 (2018) 1803151.
[40] W.B. Swanson, M. Omi, Z. Zhang, H.K. Nam, Y. Jung, G. Wang, P.X. Ma, N. E. Hatch, Y. Mishina, Macropore design of tissue engineering scaffolds regulates mesenchymal stem cell differentiation fate, Biomaterials 272 (2021) 120769.
[41] V. Karageorgiou, D. Kaplan, Porosity of 3D biomaterial scaffolds and osteogenesis, Biomaterials 26 (2005) 5474–5491.
[42] L. Wu, X. Pei, B. Zhang, Z. Su, X. Gui, C. Gao, L. Guo, H. Fan, Q. Jiang, L. Zhao, 3D-printed HAp bone regeneration scaffolds enable nano-scale manipulation of cellular mechanotransduction signals, Chem. Eng. J. 455 (2023) 140699.
[43] D.D. Deligianni, N.D. Katsala, P.G. Koutsoukos, Y.F. Missirlis, Effect of surface roughness of hydroxyapatite on human bone marrow cell adhesion, proliferation, differentiation and detachment strength, Biomaterials 22 (2000) 87–96.
[44] A.B. Faia-Torres, S. Guimond-Lischer, M. Rottmar, M. Charnley, T. Goren, K. Maniura-Weber, N.D. Spencer, R.L. Reis, M. Textor, N.M. Neves, Differential regulation of osteogenic differentiation of stem cells on surface roughness gradients, Biomaterials 35 (2014) 9023–9032.
[45] L. Wan, L. Lu, T. Zhu, Z. Liu, R. Du, Q. Luo, Q. Xu, Q. Zhang, X. Jia, Bulk erosion degradation mechanism for poly (1, 8-octanediol-co-citrate) elastomer: an in vivo and in vitro investigation, Biomacromolecules 23 (2022) 4268–4281.
[46] O. Chaudhuri, L. Gu, D. Klumpers, M. Darnell, S.A. Bencherif, J.C. Weaver, N. Huebsch, H.-p. Lee, E. Lippens, G.N. Duda, Hydrogels with tunable stress relaxation regulate stem cell fate and activity, Nat. Mater. 15 (2016) 326–334.
[47] W.R. Legant, J.S. Miller, B.L. Blakely, D.M. Cohen, G.M. Genin, C.S. Chen, Measurement of mechanical tractions exerted by cells in three-dimensional matrices, Nat. Methods 7 (2010) 969–971.
[48] A.K. Gaharwar, I. Singh, A. Khademhosseini, Engineered biomaterials for in situ tissue regeneration, Nat. Rev. Mater. 5 (2020) 686–705.
[49] F. Wang, X. Cai, Y. Shen, L. Meng, Cell–scaffold interactions in tissue engineering for oral and craniofacial reconstruction, Bioact. Mater. 23 (2023) 16–44.
[50] K.K. Moncal, H. Gudapati, K.P. Godzik, D.N. Heo, Y. Kang, E. Rizk, D.J. Ravnic, H. Wee, D.F. Pepley, V. Ozbolat, Intra-operative bioprinting of hard, soft, and hard/soft composite tissues for craniomaxillofacial reconstruction, Adv. Funct. Mater. 31 (2021) 2010858.
[51] E. Dondossola, P. Friedl, Host responses to implants revealed by intravital microscopy, Nat. Rev. Mater. 7 (2022) 6–22.
[52] L. Davenport Huyer, S. Pascual-Gil, Y. Wang, S. Mandla, B. Yee, M. Radisic, Advanced strategies for modulation of the material–macrophage interface, Adv. Funct. Mater. 30 (2020) 1909331.
[53] G. Turnbull, J. Clarke, F. Picard, P. Riches, L. Jia, F. Han, B. Li, W. Shu, 3D bioactive composite scaffolds for bone tissue engineering, Bioact. Mater. 3 (2018) 278–314.
[54] X. Gui, Z. Peng, P. Song, L. Chen, X. Xu, H. Li, P. Tang, Y. Wang, Z. Su, Q. Kong, 3D printing of personalized polylactic acid scaffold laden with GelMA/autologous auricle cartilage to promote ear reconstruction, Bio-Design and Manufacturing 6 (2023) 451–463.
[55] B. Conrad, C. Hayashi, F. Yang, Gelatin-based microribbon hydrogels support robust MSC osteogenesis across a broad range of stiffness, ACS Biomater. Sci. Eng. 6 (2020) 3454–3463.
[56] R.J. Miron, D.D. Bosshardt, Multinucleated giant cells: good guys or bad guys? Tissue Eng. B Rev. 24 (2018) 53–65.
[57] C.-Y. Chen, P.-H. Tsai, Y.-H. Lin, C.-Y. Huang, J.H. Chung, G.-Y. Chen, Controllable graphene oxide-based biocompatible hybrid interface as an anti-fibrotic coating for metallic implants, Materials Today Bio 15 (2022) 100326.
[58] H. Bai, C. Li, X. Wang, G. Shi, On the gelation of graphene oxide, J. Phys. Chem. C 115 (2011) 5545–5551.
[59] S. Yin, W. Zhang, Z. Zhang, X. Jiang, Recent advances in scaffold design and material for vascularized tissue-engineered bone regeneration, Adv. Healthcare Mater. 8 (2019) 1801433.
[60] J. Park, Y.S. Kim, S. Ryu, W.S. Kang, S. Park, J. Han, H.C. Jeong, B.H. Hong, Y. Ahn, B.S. Kim, Graphene potentiates the myocardial repair efficacy of mesenchymal stem cells by stimulating the expression of angiogenic growth factors and gap junction protein, Adv. Funct. Mater. 25 (2015) 2590–2600.
[61] M.H. Norahan, M. Amroon, R. Ghahremanzadeh, M. Mahmoodi, N. Baheiraei, Electroactive graphene oxide-incorporated collagen assisting vascularization for cardiac tissue engineering, J. Biomed. Mater. Res. 107 (2019) 204–219.
[62] J.M. Anderson, A. Rodriguez, D.T. Chang, Foreign body reaction to biomaterials, Semin. Immunol. 20 (2008) 86–100.
[63] R. Sridharan, A.R. Cameron, D.J. Kelly, C.J. Kearney, F.J. O'Brien, Biomaterial based modulation of macrophage polarization: a review and suggested design principles, Mater. Today 18 (2015) 313–325.
[64] P. Graney, S. Ben-Shaul, S. Landau, A. Bajpai, B. Singh, J. Eager, A. Cohen, S. Levenberg, K. Spiller, Macrophages of diverse phenotypes drive vascularization of engineered tissues, Sci. Adv. 6 (2020) eaay6391.
[65] W. Wang, K.W. Yeung, Bone grafts and biomaterials substitutes for bone defect repair: a review, Bioact. Mater. 2 (2017) 224–247.
[66] H. Shi, Z. Zhou, W. Li, Y. Fan, Z. Li, J. Wei, Hydroxyapatite based materials for bone tissue engineering: a brief and comprehensive introduction, Crystals 11 (2021) 149.
[67] D.G. Castner, B.D. Ratner, Proteins controlled with precision at organic, polymeric, and biopolymer interfaces for tissue engineering and regenerative medicine, Principles of Regenerative Medicine 523–534 (2019).
[68] C.M. Girish, A. Sasidharan, G.S. Gowd, S. Nair, M. Koyakutty, Confocal Raman imaging study showing macrophage mediated biodegradation of graphene in vivo, Adv. Healthcare Mater. 2 (2013) 1489–1500.
[69] J. Pan, H. Li, K. Jin, H. Jiang, K. Li, Y. Tang, Z. Liu, K. Zhang, K. Chen, Z. Xu, Periosteal topology creates an osteo-friendly microenvironment for progenitor cells, Materials Today Bio 18 (2023) 100519.
[70] S.J. Roberts, N. Van Gastel, G. Carmeliet, F.P. Luyten, Uncovering the periosteum for skeletal regeneration: the stem cell that lies beneath, Bone 70 (2015) 10–18.
[71] R. Tevlin, M. Griffin, K. Chen, M. Januszyk, N. Guardino, A. Spielman, S. Walters, G.E. Gold, C.K. Chan, G.C. Gurtner, Denervation during mandibular distraction osteogenesis results in impaired bone formation, Sci. Rep. 13 (2023) 2097.
[72] E.Q.M. Souza, A.E.C. Klaus, B.F.E. Santos, M.C. da Costa, E. Ervolino, D.C. de Lima, L.A. Fernandes, Evaluations of hydroxyapatite and bioactive glass in the repair of critical size bone defects in rat calvaria, Journal of Oral Biology and Craniofacial Research 10 (2020) 422–429.
[73] D. Qiu, C. Cao, A. Prasopthum, Z. Sun, S. Zhang, H. Yang, Z. Xu, J. Tao, F. Ai, J. Yang, Elucidating osseointegration in vivo in 3D printed scaffolds eliciting different foreign body responses, Materials Today Bio 22 (2023) 100771.
[74] D. Holl, W.F. Hau, A. Julien, S. Banitalebi, J. Kalkitsas, S. Savant, E. Llorens-Bobadilla, Y. Herault, G. Pavlovic, M. Amiry-Moghaddam, Distinct origin and

region-dependent contribution of stromal fibroblasts to fibrosis following traumatic injury in mice, Nat. Neurosci. 1–14 (2024).
[75] U. Lendahl, L. Muhl, C. Betsholtz, Identification, discrimination and heterogeneity of fibroblasts, Nat. Commun. 13 (2022) 3409.
[76] G. Zhu, T. Zhang, M. Chen, K. Yao, X. Huang, B. Zhang, Y. Li, J. Liu, Y. Wang, Z. Zhao, Bone physiological microenvironment and healing mechanism: basis for future bone-tissue engineering scaffolds, Bioact. Mater. 6 (2021) 4110–4140.
[77] A.E. Jakus, A.L. Rutz, S.W. Jordan, A. Kannan, S.M. Mitchell, C. Yun, K.D. Koube, S. C. Yoo, H.E. Whiteley, C.-P. Richter, Hyperelastic "bone": a highly versatile, growth factor–free, osteoregenerative, scalable, and surgically friendly biomaterial, Sci. Transl. Med. 8 (2016), 358ra127-358ra127.
[78] M. Fontcuberta-Rigo, M. Nakamura, P. Puigbò, Phylobone: a comprehensive database of bone extracellular matrix proteins in human and model organisms, Bone Research 11 (2023) 44.
[79] M. Zhang, R. Lin, X. Wang, J. Xue, C. Deng, C. Feng, H. Zhuang, J. Ma, C. Qin, L. Wan, 3D printing of Haversian bone–mimicking scaffolds for multicellular delivery in bone regeneration, Sci. Adv. 6 (2020) eaaz6725.
[80] X. Xue, Y. Hu, S. Wang, X. Chen, Y. Jiang, J. Su, Fabrication of physical and chemical crosslinked hydrogels for bone tissue engineering, Bioact. Mater. 12 (2022) 327–339.
[81] J. Guo, X. Tian, D. Xie, K. Rahn, E. Gerhard, M.L. Kuzma, D. Zhou, C. Dong, X. Bai, Z. Lu, Citrate-based tannin-bridged bone composites for lumbar fusion, Adv. Funct. Mater. 30 (2020) 2002438.
[82] J.M. Aamodt, D.W. Grainger, Extracellular matrix-based biomaterial scaffolds and the host response, Biomaterials 86 (2016) 68–82.
[83] K.H. Vining, D.J. Mooney, Mechanical forces direct stem cell behaviour in development and regeneration, Nat. Rev. Mol. Cell Biol. 18 (2017) 728–742.
[84] J.H. Lee, Y.C. Shin, S.-M. Lee, O.S. Jin, S.H. Kang, S.W. Hong, C.-M. Jeong, J. B. Huh, D.-W. Han, Enhanced osteogenesis by reduced graphene oxide/hydroxyapatite nanocomposites, Sci. Rep. 5 (2015) 18833.
[85] W. Nie, C. Peng, X. Zhou, L. Chen, W. Wang, Y. Zhang, P.X. Ma, C. He, Three-dimensional porous scaffold by self-assembly of reduced graphene oxide and nano-hydroxyapatite composites for bone tissue engineering, Carbon 116 (2017) 325–337.
[86] J. Loeffler, G.N. Duda, F.A. Sass, A. Dienelt, The metabolic microenvironment steers bone tissue regeneration, Trends Endocrinol. Metabol. 29 (2018) 99–110.
[87] N. Van Gastel, G. Carmeliet, Metabolic regulation of skeletal cell fate and function in physiology and disease, Nat. Metab. 3 (2021) 11–20.
[88] I.A. Choi, A. Umemoto, M. Mizuno, K.-H. Park-Min, Bone metabolism–an underappreciated player, npj Metabolic Health and Disease 2 (2024) 12.
[89] S.K. Wculek, G. Dunphy, I. Heras-Murillo, A. Mastrangelo, D. Sancho, Metabolism of tissue macrophages in homeostasis and pathology, Cell. Mol. Immunol. 19 (2022) 384–408.
[90] J. Löffler, A. Noom, A. Ellinghaus, A. Dienelt, S. Kempa, G.N. Duda, A comprehensive molecular profiling approach reveals metabolic alterations that steer bone tissue regeneration, Commun. Biol. 6 (2023) 327.
[91] K. Wang, J. Ruan, H. Song, J. Zhang, Y. Wo, S. Guo, D. Cui, Biocompatibility of graphene oxide, Nanoscale Res. Lett. 6 (2011) 1–8.